Proceedings of the ASME 2024
Pressure Vessels & Piping Conference
PVP2024
July XX-XX, 2024, - , - , USA

PVP2024-123237

STATE-DEPENDENT SEISMIC FRAGILITY FUNCTIONS FOR BOLTED FLANGE JOINTS ON SPECIAL-RISK INDUSTRIAL SUBSTRUCTURES

Chiara Nardin[1], Oreste S. Bursi[1], Marco Broccardo[1], Stefano Marelli[2]

[1]University of Trento, Trento, Italy
[2]ETH Zürich, Zürich, Switzerland

ABSTRACT

Seismic vulnerability assessment of industrial plants and process equipment has gained attention lately. However, the complexity of the problem and its modelling, combined with a general scarcity of available data on industrial systems, contributed to limiting or developing risk assessment methods based on extremely simplified models. On these premises, a new methodology that combines limited data from finite element FE models with cutting-edge machine learning techniques is developed to generate state-dependent fragility functions for critical components mounted on archetypical industrial substructure modules. Specifically, referring to the classical forward uncertainty quantification scheme, a physics-informed FE model, calibrated on the results of a comprehensive shake table test campaign of a real-scale industrial braced-frame BF steel substructure, is considered. Time histories of seismic event sequences generated by a site-based ground motion model compose the input provided to the FE model. The uncertainty is then propagated through Monte Carlo analysis on inexpensive-to-run polynomial chaos expansion (PCE) metamodels set for each starting damage level condition measure. As a result, empirical state-dependent fragilities are evaluated, assuming the lognormal distribution.

Keywords: industrial facilities; piping; modelling; seismic loading; earthquakes; shaking-table

1. INTRODUCTION

1.1 State of the art

The assessment of vulnerability and seismic risk for industrial components is pivotal for modern probabilistic seismic risk evaluation. The PEER Performance-Based Earthquake Engineering (PBEE) framework has become widely recognized for its versatile formulation. Indeed, it builds upon the total probability theorem to combine probabilistic seismic hazard analysis (PSHA) with fragility, damage, and loss analysis. While fragility curves play a key role in linking seismic hazard and structural modelling, recent research has predominantly focused on characterizing damage transitions from pristine to severe states for structures subjected to a single ground motion, see [1]-[2]-[3]. However, there is a notable gap in research concerning state-dependent fragility modelling, which is essential for capturing damage accumulation due to sequential seismic events. The compounding effects of damage accumulation, evident in events like Wenchuan (2008), Tohoku (2011), and central Italy (2016), underscore the importance of accurately representing irreversible damage for reliable risk assessment. Recent studies by Abdelnaby et al. [4] and Kassem et al. [5] have investigated the effects of sequential seismic events on the performance of reinforced concrete frames, demonstrating significant differences in seismic loss assessment.

Furthermore, the selection of ground motions for event sequences has been subject to thorough studies, with Shokrabadi et al. [6] recommending the use of seismic sequences (SS) of main-shock (MS) and after-shock (AS) record pairs. In the context of non-linear structural response simulations, advances have allowed more accurate modeling of complex systems and non-structural components (NSCs). However, the coupling effects between the main structure and NSCs, especially in industrial plants, pose challenges due to the prohibitive cost of predictive non-linear time history analyses (NLTHA) for fragility analysis, which requires a large number of simulations.

To address these challenges, researchers have turned to surrogate modelling techniques, such as artificial neural networks [7], hierarchical Kriging [8], polynomial chaos expansions (PCE) [9], and support vector machines [10]. These surrogate models alleviate the computational burden associated with NLTHA and enable efficient estimation of fragility functions. The computational efficiency of surrogate models, after training, allows for millions of model evaluations per second, facilitating empirical fragility function estimation.

1.2 Scope

In this context, the paper introduces the implementation of an innovative framework for state-dependent seismic fragility assessment applied to a critical industrial process component. Section 2 outlines the heuristics of this novel framework, which integrates data from a limited number of intricate and costly sequential non-linear time history analyses (NLTHA) with polynomial chaos expansion (PCE) meta-modelling techniques. Then, Section 3 delves into the case study of the industrial SPIF mock-up, investigating the process of setting and deriving PCE-based state-dependent fragilities. Finally, Section 4 examines the main results and outlines future research directions.

2. METHODOLOGY FOR SEISMIC STATE-DEPENDENT FRAGILITY ASSESSMENT

State-dependent fragility curves are defined as a class of fragility curves conditioned not only by a measure of seismic intensity IM, but also by the initial state of damage DSi of the structure, see Iervolino et al. [11]. Hence, state-dependent fragilities enable the assessment of the vulnerability of a system that has already experienced damage, as defined by the generalised equation:

$$\begin{aligned} &\mathbb{P}\left[DS_j \middle| DS_i,\, IM = im\right] = \\ &\quad = \mathbb{P}\left[DS \geq DS_j \middle| DS_i,\, im\right] - \mathbb{P}\left[DS \geq DS_{j+1} \middle| DS_i,\, im\right] \end{aligned} \tag{1}$$

for $j>i$ and i indices ranging among the identified and most severe damage limit states. Figure 1(a) showcases the generalized transition probability state matrix for a system with three possible levels of damage, i.e., $DS0$ to $DS2$. Each row of the matrix represents the initial damage state or level; whilst each column indicates the final damage state. Each bin represents the transition probability between the initial (row) and final (column) state, including the permanence within the same level.

Transition to damage state DS_j

Initial damage state DS_i	I S_0	DS_1	DS_2
DS_0	$1-\mathbb{P}_{01}-\mathbb{P}_{02}$	$\mathbb{P}[DS \geq DS_1 \vert\, DS_0, IM]$ $-\,\mathbb{P}[DS \geq DS_2 \vert\, DS_0, IM]$	$\mathbb{P}[DS \geq DS_2 \vert\, DS_0, IM]$
DS_1	×	$1-\mathbb{P}_{12}$	$\mathbb{P}[DS \geq DS_2 \vert\, DS_1, IM]$
DS_2	×	×	1

FIGURE 1: Transition state matrix.

To sufficiently populate each position of the transition matrix, i.e., to perform state-dependent fragility analysis, a huge number of sequential seismic NLTHAs is needed. The structural and non-structural system performances are then clustered according to the reference damage metric. Hence, either empirical or parametric fragility functions are derived, conditioned on the initial damage state condition and the IM of the seismic input.

However, the steep computational requirements of an extensive set of sequential NLTHAs generally hinder this direct derivation of state-dependent fragilities. Thus, cost-effective metamodels for each initial damage level – i.e., rows of the transition matrix of Figure 1(a) – are tailored on the physics-informed problem and trained on a much smaller dataset. Specifically, to keep down the computational burden even further, PCA – principal component analysis – on the seismic input of the cost-effective PCE metamodels for the Monte Carlo sequential NLTHAs is performed.

3. DERIVATION OF STATE-DEPENDENT FRAGILITIES FOR BOLTED FLANGE JOINTS

3.1 Description of the SPIF case studio

The SPIF project was conceived to test the seismic performance of archetypal industrial mock-ups and mounted process components by means of shaking table. The tested mock-up comprises a load-bearing steel framework supporting horizontal and vertical tanks, a cabinet, and piping installations. Figure 2 illustrates the SPIF mock-up at the EUCENTRE Laboratory, Italy. The mock-up features a three-story steel grade S355 structure, where the horizontal floors consist solely of crossbeams attached with hinges to the frame beams, providing flexibility. The structure has plan dimensions of 3.7 m x 3.7 m, with a storey height of 3.1 m. The system designed to withstand horizontal forces consists of two moment-resisting frames (MRFs) in the direction of seismic excitation and two braced frames (BFs) in the transverse direction. The BFs are equipped with tension/compression bracings with a circular cross-section to limit displacements and torsional effects. The two MRFs are interconnected through the BFs and crossbeams, secured to the frame beams via a fin plate-type connection.

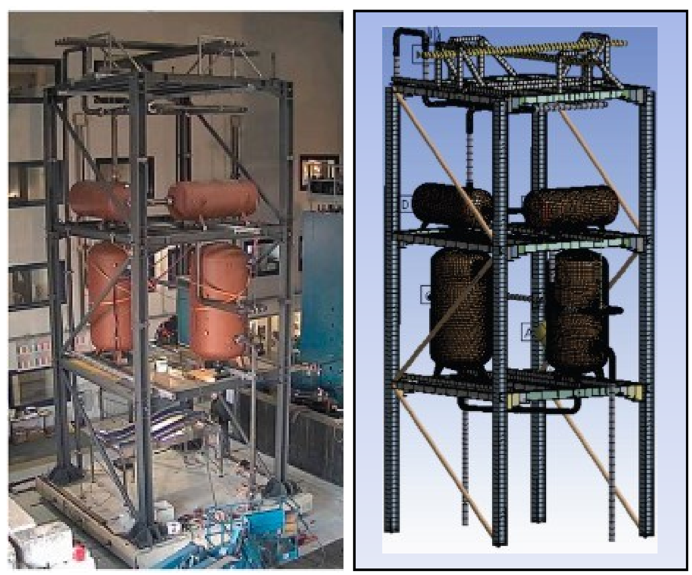

FIGURE 2: (a) Photo of the lateral view of the SPIF mock-up; (b) refined FE model.

The secondary components within the industrial structure encompass pipes, elbows, tanks, bolted flange joints (BFJs), tee-pipe joints, a conveyor, and a cabinet. Specifically, four unpressurized tanks, steel S235 – JRG2, were placed according to common practice. The tanks are interconnected through a piping system of DN 100 pipes, with thickness of 3.6 mm. The piping arrangement includes straight sections, elbows, and tee pipe joints, all made of steel P235. To detect any potential fluid leaks, four branches of pipes (Pos.#1, #3, #4, #6) were filled with water and pressurized. Critical details of the piping system are represented by bolted flange joints (BFJs). Those are DN100-PN16 joints with loose flanges and collars on one side and solid flanges on the other side, sealed by M16x8 and 2 mm aramid NBR gasket. The internal pressure is approximately 20 bar, with applied tightening torque of 80 Nm [12].

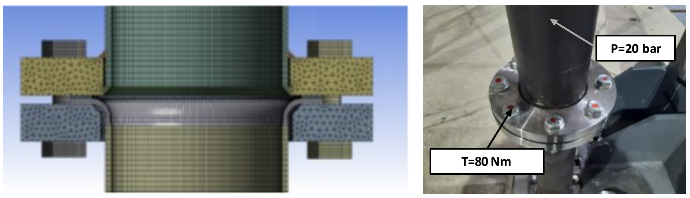

FIGURE 3: FE model and real installed BFJ

3.2 The FEM of SPIF

Concerning the finite element model (FEM) of the industrial mockup, the main structure, i.e., the two MRFs and the flexible diaphragm, is modelled with Euler-Bernoulli elements, while the diagonals of the BFs (in a transversal direction with respect to the seismic action) with truss-type non-linear tension only elements. The four tanks and the cabinet are modelled with stick models. Equivalent translational and rotational masses, along with equivalent stiffness, are assigned to nodes and elements of the simplified stick models. Except for the pipe element Pos#6, realized with shell-thin elements, the piping layout is modelled through beam-equivalent elements. For more details, see [13]. Special attention was devoted to FE modelling of refined and equivalent BFJs, as in Figure 3. On the results of refined FEM, equivalent rotational and translational stiffnesses were assigned to simplified stick models to mimic the reaction at the level of the flanges.

3.3 NLTHA of seismic sequences

Sequential non-linear time history analyses are performed on the FE model. Specifically, sequences of seismic ground motion are concatenated by sampling time histories from a huge ensemble of synthetic ground motions. Those are derived by the site-base ground motion model (GMM) of Der Kiureghian and Rezaeeian (2010) [14]. Briefly, the GMM consists of a modulated and filtered white-noise process that accounts for temporal and spectral non-linearities. It can be summarized in the following Equations:

$$a_g(t) = q(t,\hat{\alpha})\left[\frac{1}{\sigma_f(t)}\int_{-\infty}^{t} h(t-\tau,\lambda(\tau))\omega(\tau)d\tau\right] \quad (2)$$

where $\omega(\tau)$ is the white-noise process, $\sigma_f(t)$ is the standard deviation of the filtered process and $\hat{\alpha}$ is the parameter of the modulating function $q(t,\hat{\alpha})$ defined as:

$$\hat{\alpha} = \arg min_{\alpha}\left(\left|I_a(t_{45}) - \hat{I}_a(t_{45})\right| + \left|I_a(t_{95}) - \hat{I}_a(t_{95})\right|\right) \quad (3)$$

where $I_a(\cdot)$ and $\hat{I}_a(\cdot)$ define the true and estimated Arias intensity at t_{45} and t_{95} of the intensity.

Moreover, in the Eqn. (2), $h(t-\tau,\lambda(\tau)) = f(\omega_f,\dot{\omega},\zeta_f)$ represents the impulse-response function (IRF), function of $\omega_f = \omega_{mid} + \dot{\omega}_{mid}\,(t - t_{mid})$, with $\dot{\omega}_{mid}$ and ζ_f the variation of the mean frequency and the damping ratio of the filter.

Then, the GMM was deployed to generate an ensemble of 10^4 synthetic time histories. Those were randomly sampled to constitute a sequence of 5 events, as depicted in Figure 4.

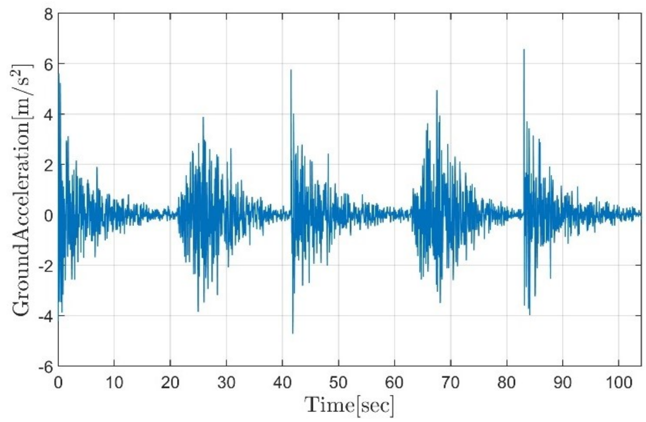

FIGURE 4: Assembled sequence of 5 synthetic ground motions, generated by the GMM of [10].

A 100 of sequences of NLTHA were performed with a computational cost of 48 hours. From these analyses, the maxima stresses of all relevant BFJs were saved and classified into two (T_u, N_u) -ultimate shear and normal resistance- leakage domain, as outlined in Figure X. Given the design couple (F_L, F_R) and the initial damage state that defines (T_u, N_u), if Eqn. (4) is not verified, then a damage state transition is recorded.

$$Y = \frac{F_L}{T_{u,DSi}} + \frac{F_{RI}}{N_{u,DSi}} \leq 1 \text{ where i } = 0,1,2 \quad (4)$$

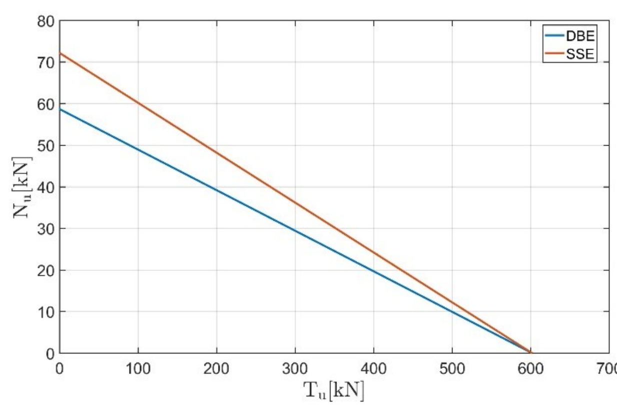

FIGURE 5: Leakage domain for initial damage state level DS_0 (DBE), DS_1 (SSE).

Specifically, in the Eqn. (4), F_L is the resultant of the shear components in the two main directions:

$$F_L = \sqrt{{F_x}^2 + {F_y}^2} \tag{5}$$

while F_R is the axial force acting on the joint (F_A) plus the contribution of the bending moment from the two main directions M_A:

$$F_R = F_A \pm \frac{4}{\phi} \cdot M_A \tag{6}$$

where ϕ indicates the bolts interaxis and $M_A = \sqrt{{M_x}^2 + {M_y}^2}$.

Finally, for the most critical BFJ at the base of the model, Table (1) gathers the transition among states after the 100 sequential analyses with percentages of the total simulations in brackets.

	DS0	DS1	DS2
DS0	272 (0.79)	39 (0.11)	34 (0.10)
DS1	0	74 (0.95)	4 (0.05)
DS2	0	0	77 (1.00)

TABLE 1: transition state matrix for BFJ Pos.#1

3.3 PCE surrogate-based fragilities

The analyses carried out on the numerical model are limited by the computational cost. To overcome this issue, surrogate models are adopted. Two key elements are derived by the NLTHA results, i.e., the input parameters *X* and the *Y* responses of the FE model. The metamodel needs to be calibrated via the Experimental Design (ED) set (which contains a percentage close to 100% of the data resulting from the analyses), then to be validated using the Validation set (populated with the remaining data) to determine the accuracy of the built metamodel. If the computational model allows one analysis to be performed in a few hours, the corresponding surrogate model performs up to 10^6 analyzes in a few seconds. Multiple IMs can be used to describe a seismic event. However, to reduce the input space, Principal Component Analysis (PCA) is performed. In this case, the dataset of input parameters *X* was reduced from 44 variables to 10 principal components (PCs). Then, the metamodel technique implemented was polynomial chaos expansions (PCE), on the probability distributions of the input parameters X_{PCA}. This method allows us to approximate the real model in the following way:

$$M(X_{PCA}) \approx \widetilde{M}(X_{PCA}) = \sum_{\alpha \in \mathbb{N}^{\mathrm{M}}} y_\alpha \psi_\alpha (X_{PCA}) \tag{7}$$

where ψ_α are basis of the polynomials, y_α are the corresponding coefficients and $\alpha = (\alpha_1, \dots, \alpha_{\mathrm{M}})$ are indexes, which represent the degree of each polynomial for each variable (the polynomials are multivariate).

Once the surrogate model is built, the validation set is used to identify the difference between the response of the meta-model Y_{PCE} and the response of the numerical model Y_{true}, as depicted in Figure (6). The good alignment of results on the 45° line demonstrates the favourable performances of the metamodel.

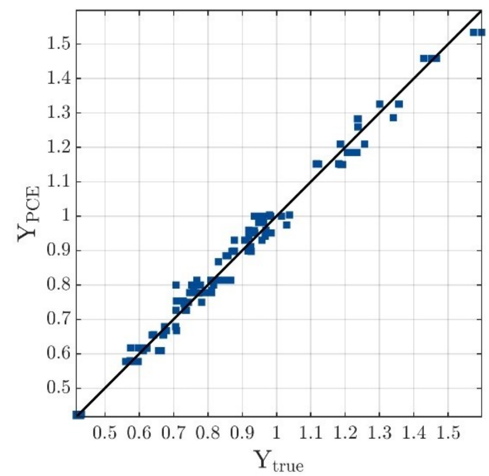

FIGURE 6: Surrogate model vs numerical model

Moreover, also the normalized empirical error ε_{emp} is calculated:

$$\varepsilon_{emp} = \frac{\sum_{i=1}^{N} \left(M\left(x^{(i)}\right) - \widetilde{M}\left(x^{(i)}\right) \right)^2}{\sum_{i=1}^{N} \left(M\left(x^{(i)}\right) - \hat{\mu}_Y \right)^2} \tag{8}$$

where $\hat{\mu}_Y$ is the average of *M*(*x*), varying the number of principal components (PCs) considered and the dimension of the experimental design data. Figure (7) gathers the results in a 3D plot: the optimal solutions can be found around 10 PCs and an experimental design size of 150 elements.

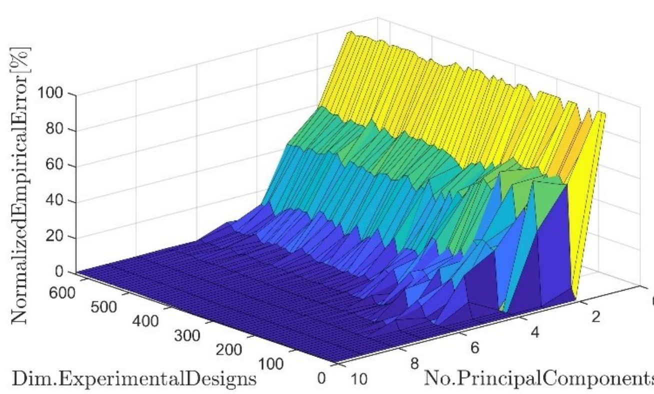

FIGURE 7: Variation of ε_{emp} varying the ED datasets and number of PCs.

For an ED of 150 elements, Figure (8) collects the dispersion of the ε_{emp}, through violin plots with different number of PCs.

As Figure (8) reveals, considering 10 PCs leads to an empirical error below the 5%. The same results are achieved for both the two implemented surrogate models, i.e., the one with initial damage state 0 and the other with initial damage state 1. Once the two models have been validated, 10^4 synthetic earthquakes are assigned that resulted in 10^4 responses. To represent the fragility functions of the BFJs, the best intensity measure (IM) must be identified. To do so, the involved criteria are efficiency and effectiveness. Efficiency refers to a measure of the total variability of the response of the model given a fixed IM; whilst effectiveness refers to the ability of an IM to identify linearity or correlations between input-outuput, see [15] for further details.

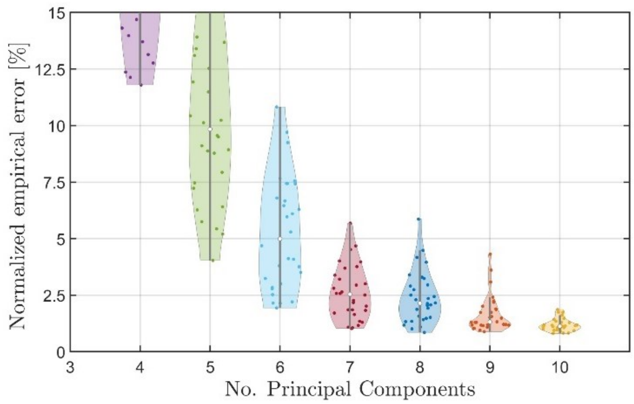

FIGURE 8: Violin plot of the dispersion of ε_{emp}.

The choice of efficiency-driven IM is pursued through β_{index} parameter, defined as:

$$\beta_{index} = \left(IQR|_{IM,x1}\right) + \left(IQR|_{IM,x2}\right) + \left(IQR|_{IM,x3}\right) \qquad (9)$$

where IQR is the inter-quantile range and IM, xi are the $25^{th} \div 50^{th} \div 75^{th}$ quantile of the IM. The most efficient IM is the one with the lowest β_{index}. Indeed, the best effectiveness-driven IM is expressed through the absolute value of the Pearson correlation coefficient:

$$|\rho_{IM,EDP}| = \left|\frac{\sum_i[(IM_i - \overline{IM}) \cdot (EDP_i - \overline{EDP})]}{\sqrt{\sum_i(IM_i - \overline{IM})^2 \cdot \sum_i(EDP_i - \overline{EDP})^2}}\right| \qquad (10)$$

Finally, to select the best IM considering efficiency and effectiveness, a new γ_{sel} coefficient is evaluated as:

$$\gamma_{sel} = \beta_{index}/|\rho_{IM,EDP}| \qquad (11)$$

For each IM and each transition state the γ_{sel} is evaluated, leading to the best suite of IMs as collected in Table 2.

Fragilities 0-0		Fragilities 0-1	
IM	γ_{sel}	IM	γ_{sel}
$S_{a,1}$	0.0455	E-ASA$_{R67}$	0.2342
$S_{d,1}$	0.0833	E-ASA$_{R80}$	0.2349
$S_{v,1}$	0.0833	$S_{d,5}$	0.2534
E-ASA$_{R80}$	0.0833	$S_{a,5}$	0.2534
$S_{d,3}$	0.1083	E-ASA$_{R100}$	0.2628

Fragilities 0-2		Fragilities 1-1		Fragilities 1-2	
IM	γ_{sel}	IM	γ_{sel}	IM	γ_{sel}
ASI	0.2006	$S_{d,1}$	0.1606	IC	0.3170
E-ASA$_{R80}$	0.2071	E-ASA$_{R80}$	0.1606	I_A	0.3527
$S_{a,1}$	0.2123	$S_{a,1}$	0.1606	ASI	0.3749
E_{cum}	0.2141	PGV	0.1613	I_{CM}	0.3788
I_A	0.2147	ASA$_{40}$	0.1629	E-ASA$_{R80}$	0.4065

TABLE 2: Optima IMs for each transition state according to γ_{sel} coefficient.

It is evident that the γ_{sel} significantly decreases for the 0-0 transition state, primarily due to the extensive amount of data for the state. Conversely, for transitions towards more severe damage states (0-1, 0-2, 1-2), this coefficient tends to increase, indicating a higher degree of IM-Υ uncorrelation and greater dispersion of Υ per assigned IM. Notably, E-ASA$_{R80}$ and ASI emerge as among the most effective IMs, ranking within the top five of the transition states.
Figure 9 depicts the fragilities functions associated to the best IM according to each damage state.

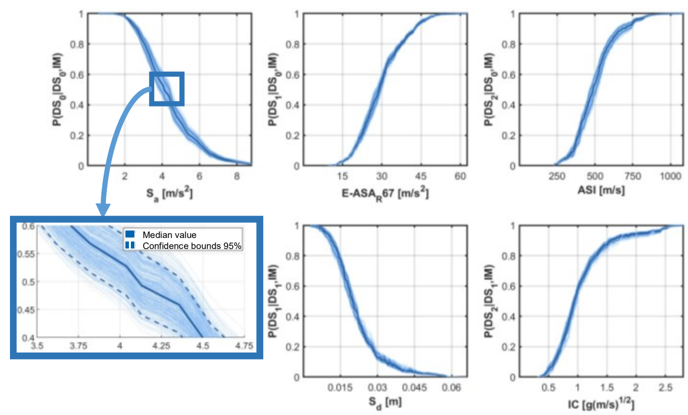

FIGURE 9: State-dependent fragility functions for the BFJ of Pos#1.

4. CONCLUSION AND OUTLOOKS

In this paper, state-dependent fragilities functions for critical industrial elements were derived. Specifically, BFJs were examined with respect to leakage damage state scenario, according to the industrial DBE and SSE definitions.
To tackle the computational burden, metamodeling techniques are adopted. This enables to consider the damage accumulation effects due do sequence of seismic events. The GMM of Der Kiureghian and Rezaeian was deployed to simulate sequences of seismic time histories, assigned to refined FE model. NLTHAs were performed to populate datasets for two PCE surrogate models, characterized by an undamaged and damaged limit state initial condition. The validation of the metamodels exhibits favourable results, as long as a sufficient number of input parameters is considered. On this line, PCA was applied

to balance the input dimensionality. Leveraging the no-cost execution of the metamodels, 10^4 simulations are performed to derive empirical state-dependent fragilities. A mixed criterion based on effectiveness and efficiency is defined to assess the optimal IM for each transition state. The innovative E-ASAR and the ASI emerge as the recurrent optimal IMs. The first one is based on the drop of frequency due to recorded damage, the second on acceleration parameters. Further analyses are needed to in-depth investigate the state-dependent fragilities behaviour and to implement recovery functions in the process.

ACKNOWLEDGEMENTS

The first three authors acknowledge the Italian Ministry of Education for the project DICAM-EXC (Departments of Excellence 2023-2027, grant L232/2016) and the National Project MUR PNRR M4C2-CN1-SPOKE 9 project HPC, Big Data and Quantum Computing.

REFERENCES

[1] Du A, Padgett JE. Investigation of multivariate seismic surrogate demand modeling for multi-response structural systems. Engineering Structures 2020; 207: 110210. doi: doi.org/10.1016/j.engstruct.2020.110210

[2] Ghosh J, Padgett JE. Aging Considerations in the Development of Time-Dependent Seismic Fragility Curves. Journal of Structural Engineering 2010; 136(12): 1497-1511. doi: 10.1061/(ASCE)ST.1943-541X.0000260

[3] Gentile R, Galasso C. Gaussian process regression for seismic fragility assessment of building portfolios. Structural Safety 2020; 87. doi: 10.1016/j.strusafe.2020.101980

[4] Abdelnaby AE. Fragility curves for RC frames subjected to Tohoku mainshock-aftershocks sequences. Journal of Earthquake Engineering 2018; 22(5): 902-920.

[5] Kassem MM, Nazri FM, Wei LJ, Tan CG, Shahidan S, Zuki SSM. Seismic fragility assessment for moment-resisting concrete frame with setback under repeated earthquakes. Asian Journal of Civil Engineering 2019; 20: 465-477.

[6] Zhang Y, Burton HV, Sun H, Shokrabadi M. A machine learning framework for assessing post-earthquake structural safety. Structural Safety 2018; 72: 1-16. doi: doi.org/10.1016/j.strusafe.2017.12.001

[7] Du A, Cai J, Li S. Metamodel-based state-dependent fragility modeling for Markovian sequential seismic damage assessment. Engineering Structures 2021; 243: 112644. doi: doi.org/10.1016/j.engstruct.2021.112644

[8] Abbiati G, Broccardo M, Abdallah I, Marelli S, Paolacci F. Seismic fragility analysis based on artificial ground motions and surrogate modeling of validated structural simulators. Earthquake Engineering & Structural Dynamics 2021; 50(9): 2314-2333. doi: doi.org/10.1002/eqe.3448

[9] Hurtado JE. Filtered importance sampling with support vector margin: A powerful method for structural reliability analysis. Structural Safety 2007; 29(1): 2-15. doi: doi.org/10.1016/j.strusafe.2005.12.002

[10] Zhu X, Broccardo M, Sudret B. Seismic fragility analysis using stochastic polynomial chaos expansions. Probabilistic Engineering Mechanics 2023; 72: 103413. doi: doi.org/10.1016/j.probengmech.2023.103413

[11] Sudret B. (2017). Surrogate modelling approaches for stochastic simulators.

[12] Nardin C., Bursi O., Paolacci F., Pavese A., Quinci G. (2022). Experimental performance of a multi-storey braced frame structure with non-structural industrial components subjected to synthetic ground motions. Earthquake Engineering & Structural Dynamics.

[13] Quinci G., Nardin C., Paolacci F., Bursi O. (2023). Modelling of non-structural components of an industrial multi-storey frame for seismic risk assessment. Bulletin of Earthquake Engineering. 21. 10.1007/s10518-023-01753-4.

[14] Rezaeian S, Der Kiureghian A. Simulation of synthetic ground motions for specified earthquake and site characteristics. Earthquake Engineering & Structural Dynamics 2010. doi: doi:10.1002/eqe.997

[15] Hariri-Ardebili, M. Amin, Saouma, V. (2016). Probabilistic seismic demand model and optimal intensity measure for concrete dams. Structural Safety. 59. 67-85. 10.1016/j.strusafe.2015.12.001.

